Applied Surface Science 517 (2020) 146214

Contents lists available at ScienceDirect

Applied Surface Science

journal homepage: www.elsevier.com/locate/apsusc

Full Length Article

Microstructural characteristics and properties of CoCrFeNiNb$_x$ high-entropy alloy coatings on pure titanium substrate by pulsed laser cladding

Kang Xiang[a], Liang-Yu Chen[b,*], Linjiang Chai[a,*], Ning Guo[c,*], Hao Wang[d]

[a] College of Materials Science and Engineering, Chongqing University of Technology, Chongqing 400054, China
[b] School of Science, Jiangsu University of Science and Technology, Zhenjiang, Jiangsu 212003, China
[c] Faculty of Materials and Energy, Southwest University, Chongqing 400715, China
[d] Nuclear Power Institute of China, Chengdu, Sichuan 610041, China

ARTICLE INFO

Keywords:
Pure titanium
Laser cladding
High-entropy alloy
CoCrFeNiNb$_x$
Phase constitution
Hardness

ABSTRACT

CoCrFeNiNb$_x$ (x = 0 or 1 at.%) high-entropy alloy (HEA) coatings with good metallurgical bonding were successfully prepared on surfaces of pure titanium sheets by pulsed laser cladding. Phase constitutions and microstructural characteristics of the HEA coatings were characterized and analyzed by combined use of X-ray diffraction, electron channeling contrast imaging, energy dispersive spectroscopy and electron backscatter diffraction techniques. Results show that the HEA coating without Nb is consisted of BCC solid-solution phase with equiaxed bulk grain morphology and Cr$_2$Ti Laves phase (C14-type hexagonal structure) with fine interdendritic lamellar morphology. After adding 1 at.% Nb, in addition to the BCC solid-solution phase and the Cr$_2$Ti Laves phase, Cr$_2$Nb Laves phase with C15-type cubic structure also appears in the interdendritic region in the HEA coating. Hardness tests reveal that the CoCrFeNiNb$_x$ HEA coatings are significantly harder than the pure titanium substrate (~122 HV). The hardness value of the HEA coating with 1 at.% Nb reaches 1008 HV, which is ~ 8.3 times that of the substrate and considerably higher than that of bulk HEAs with similar compositions. Such high hardness can be attributed to the combined contribution from solid-solution hardening, and hardening from grain refinement and Laves phases with fine lamellar morphologies.

1. Introduction

As a new type of alloy system, high-entropy alloys (HEAs) or multi-principal-element alloys (MPEAs) have attracted wide attention in recent years [1–5]. It is generally accepted that HEAs are composed of at least five major elements and the concentration of each element ranges from 5 to 35 at.% [6,7]. Since their high configuration entropy ($>$ 1.5 R and R is the gas constant) could significantly reduce the Gibbs free energy of the system, HEAs are often mainly composed of simple solid-solution phases (such as body-centered cubic (BCC) or face-centered cubic (FCC) structure) rather than intermetallic compounds or other complex brittle phases as predicted by traditional theory. A number of studies have demonstrated that HEAs with suitably designed structures and compositions possess many favorable properties, such as high strength and ductility [8–12], excellent corrosion resistance [13] and good creep resistance [14], suggesting a great application potential in many fields.

Among various metallic materials, titanium (Ti) and its alloys have been widely used in aerospace, marine, chemical and biomedical industries due to their attractive properties like high strength to density ratio, good corrosion resistance and biocompatibility [15,16]. Nevertheless, surface failure often occurs under friction conditions because of their low hardness and poor wear resistance that largely reduce service reliability [17]. The case is even worse for work pieces made of pure Ti. Hence, various surface treatments aiming at improving their wear resistance have been attempted by many researchers. As a modern surface treatment technique, laser cladding with features of easy operation, high processing efficiency and very effective property improvement is receiving increasingly attention nowadays [18–23]. It uses high-energy laser beam to melt substances coated on substrate materials, accompanied by ultrafast heating/cooling ($> 10^4$–10^6 K/s), limited thermal effect on substrate and feasible control of coating thickness (upto $>$ 1 mm). Guo et al. [24] successfully fabricated NiCrBSi and NiCrBSi/WC-Ni composite coatings on a pure Ti substrate by laser cladding and found that the coatings started to be oxidized until the temperature exceeded 650 °C, largely higher than that of the substrate, exhibiting excellent oxidation resistance at elevated temperatures. Cai et al. [25] attempted to employ the same technique to prepare a NiCrCoTiV HEA

---

* Corresponding authors.
E-mail addresses: lychen@just.edu.cn (L.-Y. Chen), chailinjiang@cqut.edu.cn (L. Chai), guoning_1000@163.com (N. Guo).

https://doi.org/10.1016/j.apsusc.2020.146214
Received 22 January 2020; Received in revised form 24 March 2020; Accepted 25 March 2020

coating on a Ti-6Al-4V substrate and demonstrated that the coating was comprised of BCC solid-solution phase and (Ni, Co)Ti_2 intermetallic compounds, jointly leading to greatly improved wear resistance. To date, however, it should be admitted that there have still been very few studies focusing on high-performance HEA coatings prepared by laser cladding on Ti and its alloys, with their specific microstructural features essentially unexplored.

In this work, a high-purity Ti sheet was selected as the substrate material, with the laser cladding technique employed to prepare CoCrFeNiNb$_x$ ($x = 0$ or 1 at.%) HEA coatings on the substrate. Phase constitutions and microstructural characteristics of the coatings were investigated in detail by multiple characterization techniques. Hardnesses of the substrate and the coatings were also examined with reasons accounting for hardness variations explored based on the revealed microstructure characteristics. These results are expected to provide an important reference for preparing high-performance HEA coatings (different from traditional ones) on Ti and its alloys to enhance their service reliability.

2. Experimental

The as-received substrate material was a pure Ti sheet (99.99% purity) after rolling and recrystallization annealing. Rectangular specimens with dimensions of 17 mm × 9 mm × 2.6 mm were cut from the as-received sheet by using a wire-cutting machine along three orthogonal directions, namely rolling (RD), transverse (TD) and normal (ND) directions, respectively. Then, 180#, 400#, 800# and 1200# silicon carbide abrasive papers and ethanol were used to treat the substrate to remove surface oxides and contaminants. Co-Cr-Fe-Ni-Nb$_x$ alloy powders (Co, Cr, Fe and Ni in equiatomic ratio while $x = 0$ and 1 at.%, denoted as Nb0 and Nb1, respectively) with 99.9% purity for each component and particle sizes between 45 and 75 μm were used as the raw powders. Such raw powders were sufficiently mixed for 10 h through a ball milling machine and then pre-placed onto the RD-TD surface of the pure Ti substrate uniformly with a thickness of 500–600 μm using polyvinyl alcohol (PVA) solvent (in 10 wt%) as a binder. Subsequently, the pre-coated specimens were dried in an oven at 120 °C for 5 h. Laser cladding was carried out in a pulsed 600 W Nd: YAG laser device with scanning along the RD direction and a 50% overlap between neighboring tracks. More detailed laser processing parameters were tabulated in Table 1. During the laser processing, a continuous flow of high-purity argon gas (flow rate 5 L min^{-1}) was used to prevent oxidation.

After the laser cladding treatment, RD-TD surfaces of the coated specimens were slightly polished by SiC abrasive papers (upto 1200#) and then subjected to X-ray diffraction (XRD, PANalytical Empyrean Series 2) examination with Cu Kα radiation (8.04 keV) at 40 kV and 40 mA (2θ ranging from 20° to 90°). Cross-sectional (TD-ND) microstructures of the coated specimens were characterized by use of electron channeling contrast (ECC) imaging and electron backscatter diffraction (EBSD) techniques in a Zeiss Sigma HD field emission gun scanning electron microscope (FEGSEM). The EBSD system consisted of a NordlysMax^2 detector (Oxford Instruments), with AZtec 2.4 and HKL Channel 5 software packages used for information acquisition and data post-processing analyses, respectively. In addition, an energy dispersive spectrometer (EDS) attached to the FEGSEM was used for analyzing local compositions of the coatings. Prior to the above microstructural characterizations, the to-be-analyzed surfaces (TD-ND) of coated specimens were mechanically ground by SiC abrasive papers to 3000# in the final step and then electro-polished in a mixed solution of 90 mL methanol and 10 mL perchloric acid at −30 °C and 14 V for 100 s. Hardnesses of the substrate and the coatings were measured on the RD-TD surfaces by use of a Vickers indentation tester (HVS-1000) with a load of 100 g and a dwelling time of 10 s (ASTM E92-82(2003)). For each specimen, more than 40 indentations at an interval of 200 μm were made to calculate an average hardness value.

3. Results

3.1. Phase constitution

Fig. 1a shows XRD patterns of the pure Ti substrate, Nb0 and Nb1 coatings. The pure Ti substrate is completely composed of α-Ti phase with a hexagonal close-packed (HCP) structure, while the Nb0 coating seems to be mainly composed of two phases: a BCC solid-solution phase and a Cr_2Ti Laves phase (C14-type). In addition to the two phases, another Laves phase (Cr_2Nb, C15-type) appears in the Nb1 coating. Fig. 1b presents enlarged profiles around the (1 1 0) peak of the BCC solid-solution phase in both the HEA coatings. One can see that the (1 1 0) peak of the BCC phase in the Nb1 coating slightly shifts left, compared to that of the Nb0 coating. According to the Bragg diffraction law, the lattice constants of the BCC phase in Nb0 and Nb1 coatings are estimated using diffraction angles corresponding to the (1 1 0) peaks to be 3.0171 Å and 3.0314 Å, respectively. Such variations of the diffraction peak angles and the lattice constants are expected to be related to local lattice distortions caused by the addition of Nb [20].

3.2. Microstructural characteristics of the pure Ti substrate

Fig. 2 shows microstructural characteristics of the pure Ti substrate (before the pulsed laser cladding) revealed by ECC imaging and EBSD techniques. From Fig. 2a, the initial microstructure of the as-received Ti sheet is comprised of equiaxed grains with relatively uniform sizes, indicting sufficient recrystallization after rolling and annealing. Since no second phases (β-Ti phase or intermetallics) are detected in the pure Ti substrate, all the equiaxed grains can be confirmed to be α-Ti after referring to the above XRD results. Fig. 2b is an EBSD inverse pole figure (IPF) map with high angle boundaries (HABs, $\theta > 15°$) and low angle boundaries (LABs, $2° < \theta < 15°$) indicated, allowing grain morphologies to be well revealed. Also from Fig. 2b, most grains are found to be colored red, which suggests that their c-axes are close to the ND. This can confirm the presence of an evident crystallographic texture. The misorientation angle distribution histogram displayed in Fig. 2c reveals that the majority of misorientation angles are higher than 15°, with only a few of them $< 15°$, consistent with the distribution of HABs and LABs displayed in Fig. 2b. By use of the linear intercept method, the average grain size of equiaxed grains in the pure Ti substrate is measured to be ~ 45.0 μm.

3.3. Microstructural characteristics of the HEA coatings

TD-ND cross-sectional views (macro morphologies) and measured compositions of Nb0 and Nb1 coatings are presented in Fig. 3. Fig. 3a and c show that the fabricated HEA coatings are dense and uniform, and an excellent metallurgical bonding is achieved between the coatings and the substrate. From Fig. 3b and d, the added alloying elements in

Table 1
Processing parameters of the pulsed laser cladding.

Laser power (W)	Scanning speed (mm·s^{-1})	Defocusing amount (mm)	Peak power (kW)	Pulse duration (ms)	Frequency (Hz)	Beam diameter (mm)	Power density (W·mm^{-2})	Linear energy density (J·mm^{-1})
100	8	+2	1	5	20	1	127.4	12.5

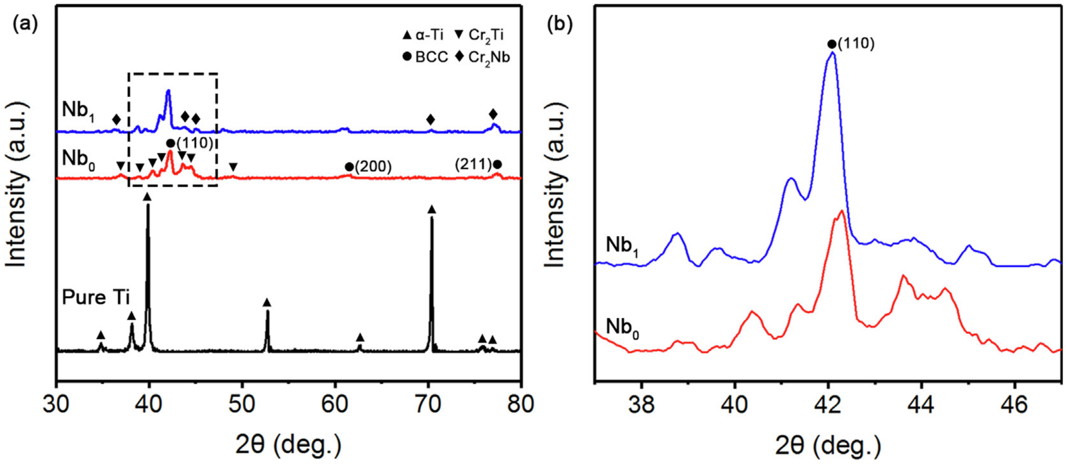

Fig. 1. (a) XRD patterns of the pure Ti substrate, Nb0 and Nb1 coatings; (b) enlarged profile around (1 1 0) peak of the BCC solid-solution phase in the coatings.

the HEA coatings are found to be generally uniform, with a higher content of Ti included in the HEA coatings as well. This demonstrates that both the pre-placed alloy powders and the pure Ti substrate are well melted and mixed during the laser cladding processing, producing good metallurgical bonding between them. Meanwhile, the high content of Ti detected in the HEA coatings indicates the occurrence of inevitable dilution of the substrate element during laser cladding. Based on a well accepted model [26], dilution rates of the Nb0 and Nb1 coatings are roughly estimated to be 53.7% and 65.9%, respectively.

ND-TD cross-sectional ECC observations of Nb0 and Nb1 coatings are exhibited in Fig. 4, allowing marked microstructural differences to be revealed between them. From Fig. 4a and b, typical dendritic (DR) morphologies can be seen for the Nb0 coating, i.e. equiaxed bulk grains enclosed by irregular-shaped interdendritic (ID) structures. A further observation for the boxed region in Fig. 4b is shown in Fig. 4c, revealing that the ID structures contain dense substructures of fine lamellae (most lamellar spacings < 150 nm). After adding Nb, three distinct morphologies can be found in the Nb1 coating (Fig. 4d). From Fig. 4e, the majority of microstructures in this coating are also comprised of equiaxed bulk grains and surrounding ID structures (coarsened), compared to those in the Nb0 coating. Fig. 4f is a magnified observation of the boxed region F in Fig. 4d, revealing bulk microstructures completely comprised of fine lamellae, similar to the morphologies of the ID structures shown in Fig. 4c. Average sizes of equiaxed bulk grains in Nb0 and Nb1 coatings are measured (> 100 grains counted for each of them using Nano Measurer 1.2 software) to be ~ 3.5 μm and ~ 2.5 μm, respectively. This suggests that the addition of 1 at.% Nb can effectively refine grains and promote the original ID structures to grow into bulk structures with internal substructures retained.

Figs. 5 and 6 present distributions of each element measured by EDS

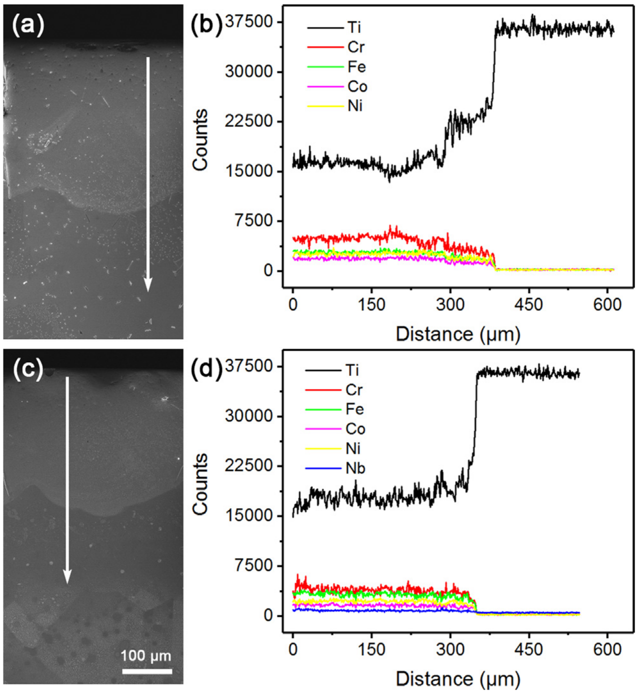

Fig. 3. (a) and (c) TD-ND cross-sectional views (macro morphologies) of Nb0 and Nb1 coatings, respectively; (b) and (d) EDS line scanning results along the arrowed paths in (a) and (c), respectively.

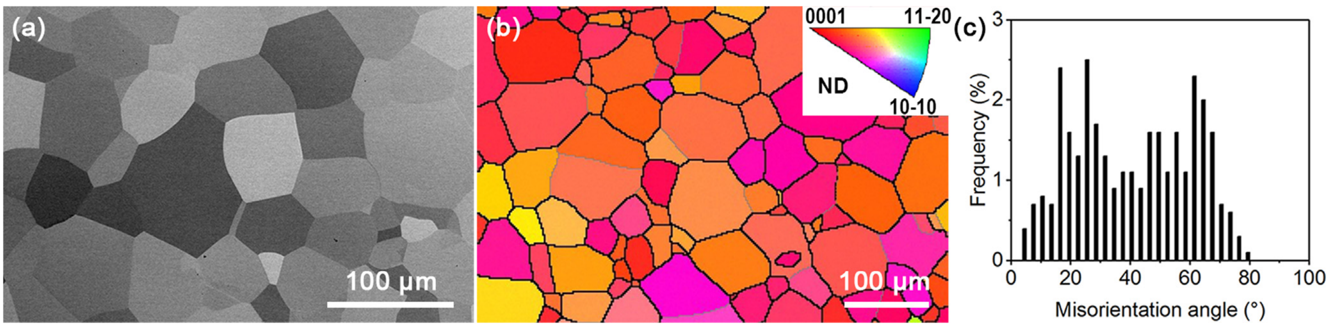

Fig. 2. Microstructural characteristics of the pure Ti substrate: (a) ECC image, (b) EBSD IPF map with black and grey lines delineating grain boundaries with θ > 15° and 2° < θ < 15°, respectively, and (c) misorientation angle distribution histogram corresponding to (b). The inset in (b) is the color code for grain orientations. (For interpretation of the references to colour in this figure legend, the reader is referred to the web version of this article.)

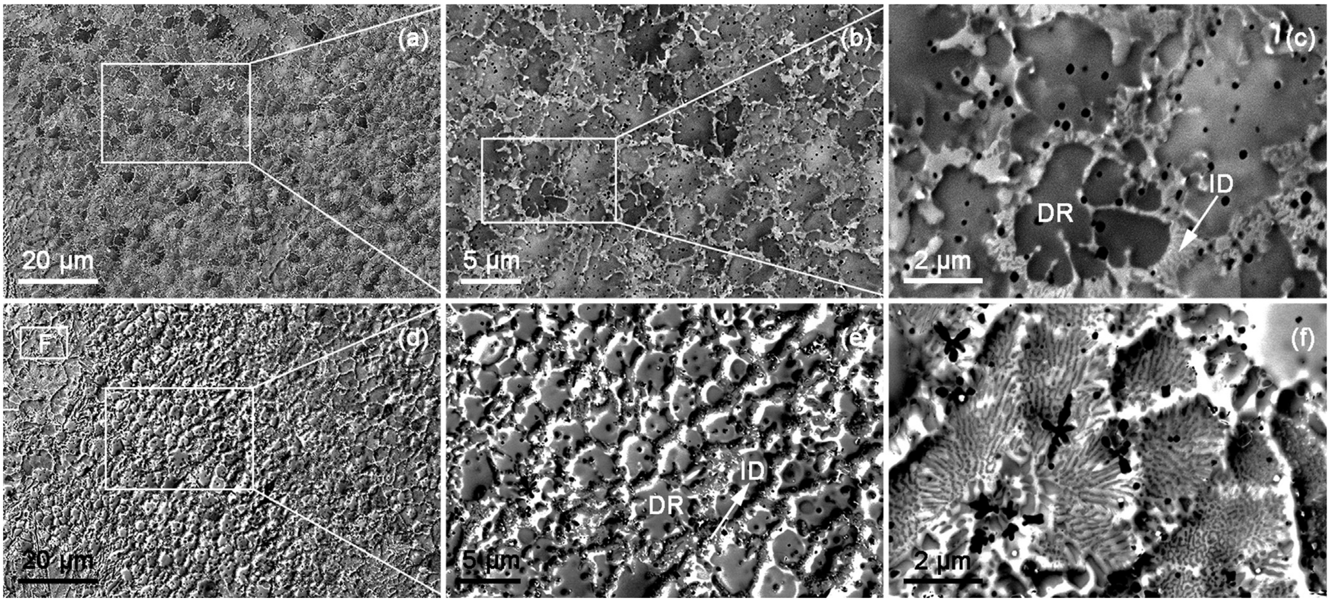

Fig. 4. ECC images of TD-ND cross-sectional views of Nb0 and Nb1 coatings: (a) low-magnification observation of the Nb0 coating, (b) magnified observation of the white box in (a), and (c) magnified observation of the white box in (b); (d) low-magnification observation of the Nb1 coating, (e) magnified observation of the white box in (d), and (f) magnified observation corresponding to region F in (d). DR and ID in figures represent dendritic and interdendritic structures, respectively.

in Nb0 and Nb1 coatings, respectively. We note that Cr and Ti prefer to be segregated in ID regions in the Nb0 coating, while other elements are evenly distributed inside the equiaxed bulk grains (Fig. 5). Combined with XRD and EDS results, the equiaxed bulk grains can be confirmed to be the BCC solid-solution phase while the ID structure corresponds to Cr_2Ti Laves phase (C14-type). After adding Nb, Fig. 6 reveals that like Cr and Ti, Nb also prefers to distribute in ID regions, with other elements remaining mainly inside the equiaxed bulk grains. After referring to the XRD results (Fig. 1), the equiaxed bulk grains in the Nb1 coating still correspond to the BCC solid-solution phase while the ID structures should be comprised of another type of Laves phase (Cr_2Nb, C15-type) along with Cr_2Ti.

Fig. 7 presents EBSD results of the BCC solid-solution phase in Nb0 and Nb1 coatings. From band contrast (BC) map shown in Fig. 7a, one can also see that the Nb0 coating is composed of equiaxed bulk grains and ID structures, consistent with direct ECC observations (Fig. 4). Fig. 7b further reveals that crystallographic orientations of the equiaxed grains are relatively scattered with no considerable preferred orientations, different from the case of the pure Ti substrate. With respect to misorientation characteristics, Fig. 7c shows that almost all grain boundaries of the BCC solid-solution phase have high misorientation angles, with essentially no low angles presented, suggesting very low residual stresses accumulated in the coating. Analyses for the Nb1 coating (Fig. 7d-f) show great microstructural similarities to those of the Nb0 coating. Nevertheless, comparisons between them can reveal that the grains in the Nb1 coating are slightly finer with increased fractions of the ID structures than in the Nb0 coating. This suggests that the addition of Nb could refine grains and produce more ID structures, consistent with the above ECC results (Fig. 4).

3.4. Surface hardness variation

Fig. 8 gives results of hardness measurements for the pure Ti substrate and the HEA coatings. Clearly, both the coatings prepared by laser cladding are much harder than the pure Ti substrate. The average hardness of the pure Ti substrate is ~ 122 HV while that of the Nb0

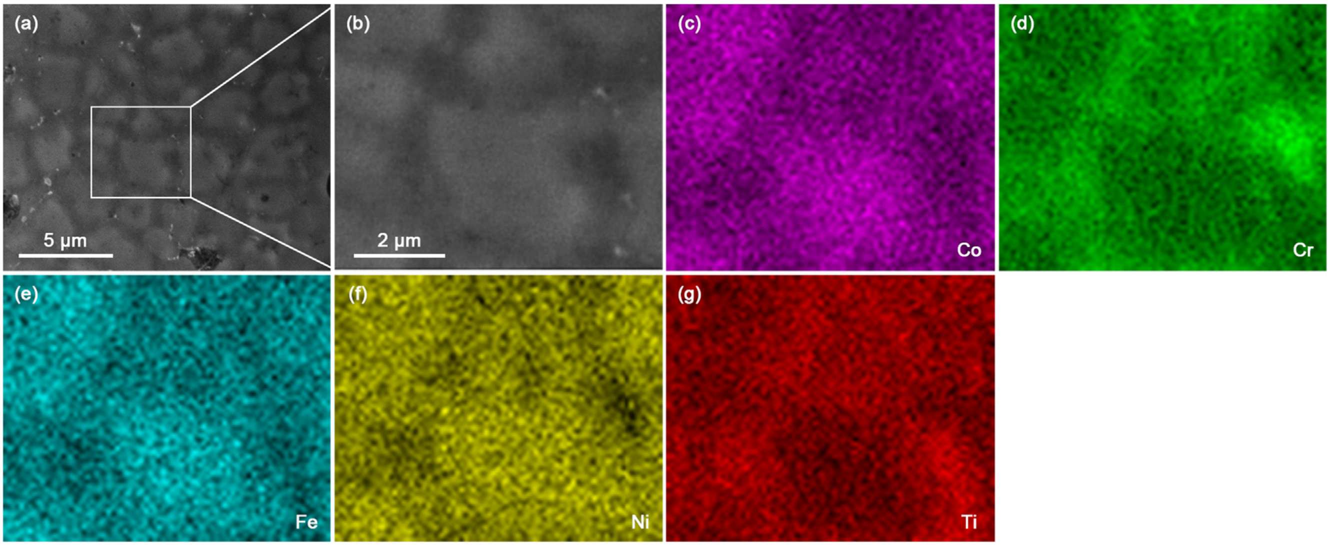

Fig. 5. EDS mapping results in the Nb0 coating: (a) and (b) morphologies of selected regions; (c) Co, (d) Cr, (e) Fe, (f) Ni and (g) Ti corresponding to (b).

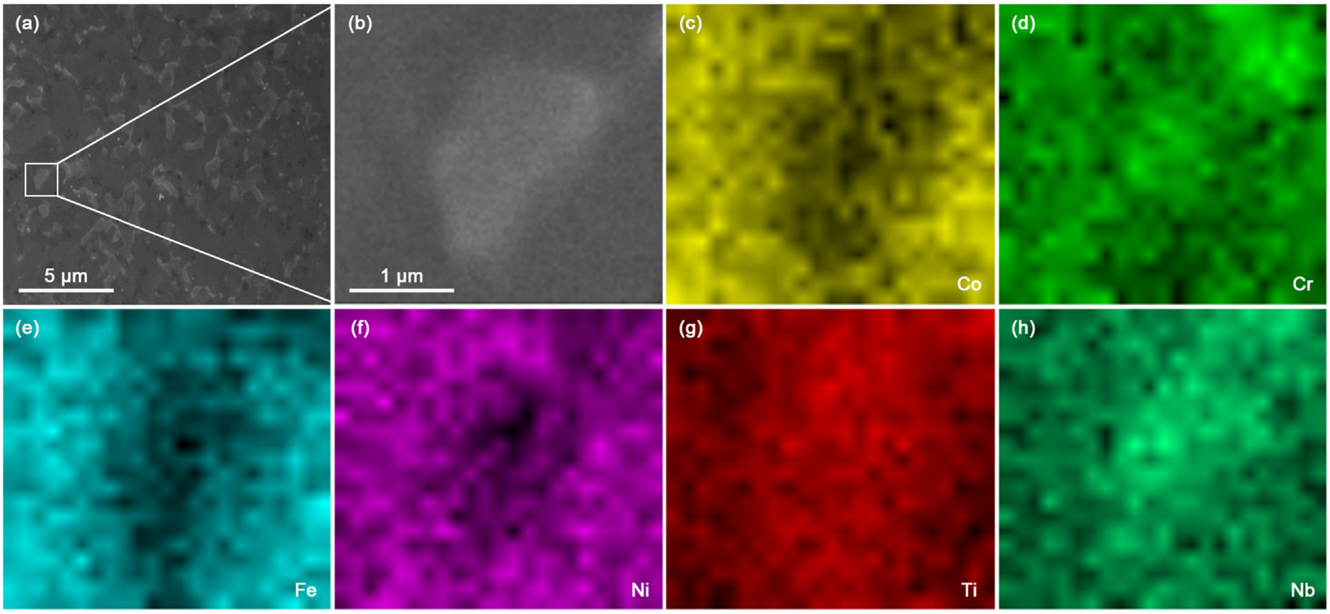

Fig. 6. EDS mapping results in the Nb1 coating: (a) and (b) morphologies of selected regions; (c) Co, (d) Cr, (e) Fe, (f) Ni, (g) Ti and (h) Nb corresponding to (b).

coating is remarkably increased to be ~ 790 HV which is ~ 6.6 times that of the substrate. After adding Nb, the average hardness of the HEA coating further goes upto 1008 HV, almost 8.3 times that of the substrate. In literature, Wang et al. [27] reported that the hardness of an as-cast CoCrFeNi bulk HEA was 150 HV with the maximum hardness of 272 HV after optimizing processing parameters, far softer than the CoCrFeNiNb$_x$ HEA coatings in this work. Jiang et al. [28] reported that an as-cast CoCrFeNiTi$_{0.5}$ bulk HEA would have a hardness of 616.8 HV, largely increased compared to Wang et al.'s work without Ti addition. Cai et al. [25] found that the hardness of an NiCrCoVTi HEA coating prepared by laser cladding on Ti-6Al-4V alloy could reach ~ 700 HV, still much lower than our results. Such a comparison suggests that our CoCrFeNiNb$_x$ HEA coatings fabricated on the pure Ti substrate own better mechanical properties. To probe reasons accounting for their high hardnesses, microstructural characteristics of the HEA coatings and their possible effects on hardness changes are comprehensively analyzed and discussed in the following.

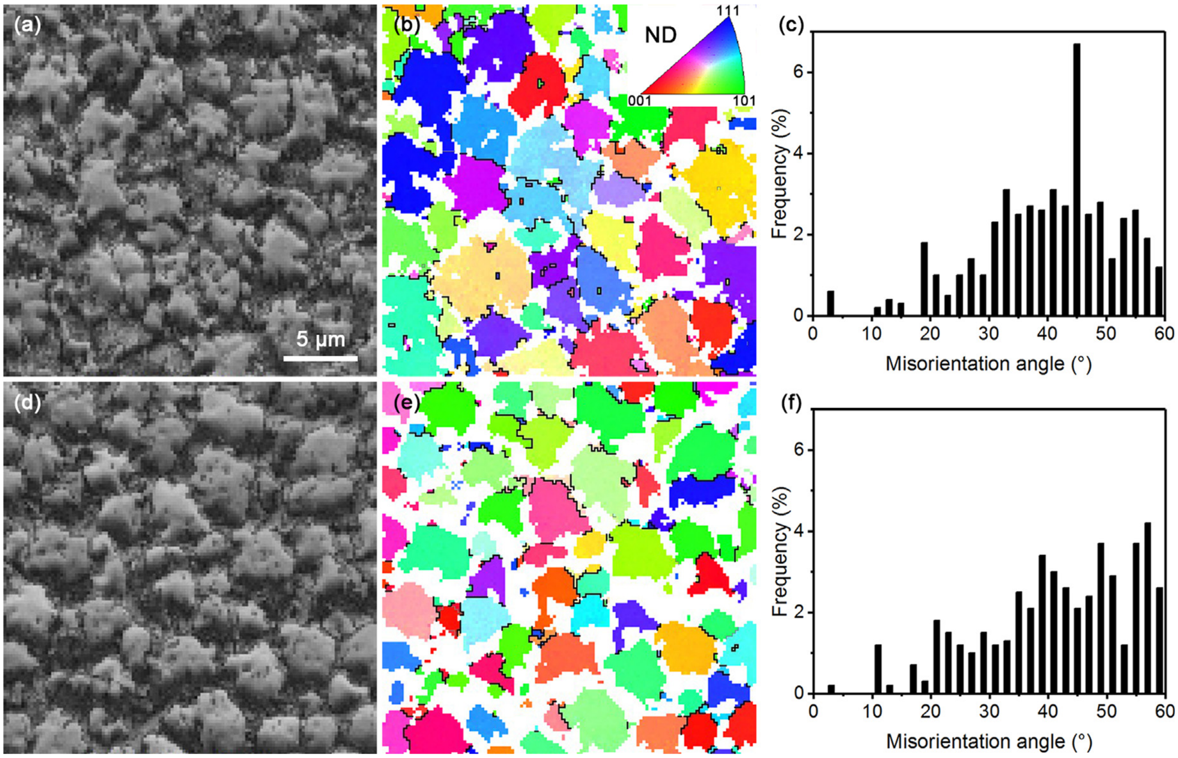

Fig. 7. (a) and (d) BC maps, (b) and (e) IPF maps, and (c) and (f) misorientation angle distribution histograms of the BCC solid-solution phase in Nb0 and Nb1 coatings, respectively.

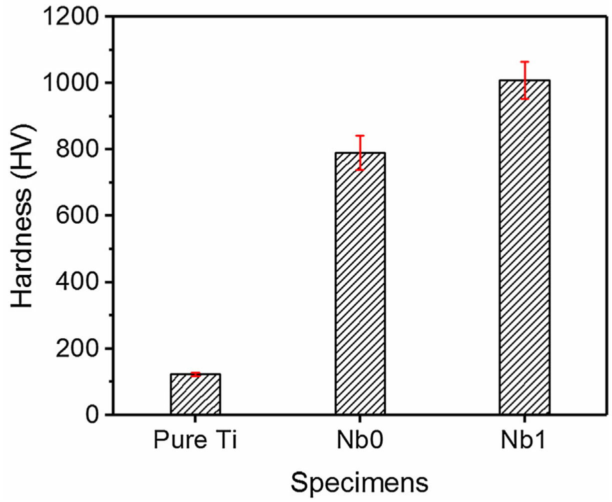

Fig. 8. Hardness values of the pure Ti substrate, Nb0 and Nb1 coatings.

4. Discussion

4.1. Reasons for variations of phase constitutions

According to the Gibbs phase rule, the number of phases after equilibrium solidification can be predicted by p = n + 1, where p is the phase number and n is the component number. After non-equilibrium solidification, however, p would be larger than n + 1 [29]. In the present work, non-equilibrium solidification occurs during the laser cladding processing due to insufficient diffusion associated with very short pulse duration (5 ms) and ultrafast cooling induced by the pulsed laser [19,30]. As a result, three non-equilibrium phases (one BCC solid-solution phase and two Laves phases) with heterogeneous microstructures are formed in the CoCrFeNiNb$_x$ HEA coatings. The total phase number is far smaller than that predicted by the Gibbs phase rule. This suggests that high entropy effect and non-equilibrium solidification caused by the laser cladding may have influenced phase formation in the HEA coatings. Earlier studies showed that the CoCrFeNi quaternary HEA usually consisted of single FCC solid-solution phase [10,31]. However, in both the Nb0 and Nb1 coatings in our work, a BCC solid-solution phase is found to be the major phase (Figs. 1 and 7) containing a considerable amount of Ti, in addition to Co, Fe and Ni (Figs. 5 and 6). Ti is known to have a much larger atomic radius than Co, Cr, Fe and Ni (Table 2) and its addition is able to promote changing the structure of this series of HEAs from FCC to BCC [32,33]. From Table 2, one can also see that electronegativity of Ti is considerably smaller than those of Co, Cr, Fe and Ni. Such differences in atomic radius and electronegativity between them would produce large local elastic strains and instability of topological systems, facilitating the formation of intermetallic compounds [34]. The case of Nb is very close to that of Ti, allowing more intermetallics compounds to be expected after adding Nb.

Further analyses on XRD and EDS results suggest that Laves phases (A_2B type) with a topological close-packed (TCP) structure are formed in the fabricated HEA coatings. Only one Laves phase, C14-type Cr_2Ti (Zn_2Mg type with an HCP structure [35]), is found in the Nb0 coating while C15-type Cr_2Nb Laves phase (Cu_2Mg type with a BCC structure) appears along with the Cr_2Ti in the Nb1 coating. Kumar et al. [36] studied polymorphic transformation of Laves phases and pointed out that Cr_2Ti and Cr_2Nb usually had the same hexagonal structure at room temperature. After annealing at elevated temperatures, the hexagonal structure could be transformed into a cubic structure. Such transformation was demonstrated to be very slow for Cr_2Ti but rather rapid for Cr_2Nb. In a recent study [37], C15-type Nb- and Cr-enriched Laves phases were confirmed to exist around sub-grain boundaries in a laser-processed Inconel 718 alloy. From the above analyses, it is known that the Cr_2Ti Laves phase maintains the C14-type hexagonal structure while the Cr_2Nb Laves phase prefers the C15-type cubic structure in the CoCrFeNiNb$_x$ coatings prepared by laser cladding.

Table 2
Values of atomic radii and electronegativity of various alloying elements [38].

Element	Co	Cr	Fe	Ni	Ti	Nb
Atomic radius (Å)	1.25	1.25	1.24	1.25	1.46	1.43
Electronegativity (Pauling)	1.88	1.66	1.83	1.91	1.54	1.60

4.2. Correlation between microstructural characteristics and hardness

As revealed in Fig. 8, hardnesses of the HEA coatings are much higher than that of the substrate and hardening is further enhanced after adding Nb. Such hardness differences and variations should be closely related to their specific microstructural characteristics. Firstly, the presence of Ti in the solid-solution phase in the CoCrFeNiNb$_x$ coatings would inevitably produce large lattice distortions, due to significant differences in atomic radius between them. As a result, BCC phase generally with higher strength/hardness than FCC phase would be preferably formed [32,39]. In both the Nb0 and Nb1 coatings, the BCC solid-solution phase is the major constitution and should be able to make a significant contribution to their high hardness. A comparison between microstructures of Nb0 and Nb1 coatings reveals that the average grain size of BCC solid-solution phase is clearly reduced after adding 1 at.% Nb (Nb0 ~ 3.5 μm versus Nb1 ~ 2.5 μm), which would bring effective hardening induced by structural refinement for the Nb1 coating.

Secondly, as a result of component segregation, Cr_2Ti and Cr_2Nb Laves phases are formed to be the ID structures in the CoCrFeNiNb$_x$ coatings. These Laves phases have TCP structures with high coordination numbers, space filling degrees, large unit cells and dislocation vectors. This will make dislocation nucleation and slipping rather difficult, leading their hardness to be as high as 8–9 GPa at room temperature [40]. It can be expected that the presence of these Laves phases could make an important contribution to hardening the HEA coatings in this work. With respect to hardening ability of Laves phases with different structures, Chen et al. [41] found that dual-phase Ti alloy containing C15-type Cr_2Ti Laves phase structure had a higher hardness than that with C14-type, suggesting a higher hardening ability for the C15-type. This may allow us to expect more significant hardening effect from C15-type Cr_2Nb Laves phase than C14-type Cr_2Ti Laves phase, which should be one reason why the Nb1 coating containing Cr_2Nb is harder than the Nb0 coating. In addition, Fig. 4 reveals that the addition of Nb promotes growth of the ID structures with a fine lamellar morphology. Recent work [42,43] has confirmed that eutectic structures with a similar lamellar morphology to those in our study were more beneficial than equiaxed bulk grains to strength and hardness of CoCrFeNiNb$_x$ bulk HEAs. More fine lamellar structures appeared in the Nb1 coating should have also made a definite contribution to its higher hardness.

As mentioned earlier, the CoCrFeNiNb$_x$ coatings prepared by laser cladding in this work are found to have much higher hardnesses than bulk HEAs with similar compositions. For example, an as-cast CoCrFeNiTi$_{0.5}$ bulk HEA prepared by vacuum induction melting was reported to have a hardness of 616.8 HV and typical grain sizes of tens of micrometers [28]. Comparatively, the grains in both Nb0 and Nb1 coatings are greatly reduced (only a few micrometers), which should be resulted from the laser-induced rapid solidification and bring grain refinement-related hardening effects. Meanwhile, such non-equilibrium solidification is able to increase solubility limits of various elements and enhance solid-solution strengthening/hardening [19,44]. From the above analyses, the excellent mechanical property (high hardness) of the CoCrFeNiNb$_x$ HEA coatings fabricated by the pulsed laser cladding on the pure Ti substrate could be ascribed to the combined contribution from solid-solution hardening, and hardening from grain refinement and Laves phases with fine lamellar morphologies.

5. Conclusions

(1) CoCrFeNiNb$_x$ (x = 0 or 1 at.%) HEA coatings with good metallurgical bonding were successfully fabricated on surfaces of the pure Ti substrate using pulsed laser cladding.
(2) Nb0 coating is consisted of BCC solid-solution phase with equiaxed bulk grain morphology and Cr_2Ti Laves phase (C14-type hexagonal structure) with fine interdendritic lamellar morphology. After adding 1 at.% Nb, in addition to the BCC solid-solution phase and the Cr_2Ti Laves phase, Cr_2Nb Laves phase with C15-type cubic structure also appears in the interdendritic region.
(3) The Nb0 and Nb1 coatings have hardness values of ~ 790 and ~ 1008 HV, respectively, significantly higher than that of the pure titanium substrate (~122 HV). Comprehensive analyses reveal that such high hardness can be attributed to the combined contribution from solid-solution hardening, and hardening from grain refinement and Laves phases with fine lamellar morphologies.

CRediT authorship contribution statement

Kang Xiang: Writing - original draft, Investigation, Software. **Liang-Yu Chen:** Formal analysis, Writing - review & editing, Funding acquisition. **Linjiang Chai:** Conceptualization, Writing - review & editing, Supervision, Funding acquisition. **Ning Guo:** Writing - review & editing, Supervision. **Hao Wang:** Methodology, Writing - review & editing.

Declaration of Competing Interest

The authors declare that they have no known competing financial interests or personal relationships that could have appeared to influence the work reported in this paper.

Acknowledgments

This work was financially supported by the Fundamental and Cutting-Edge Research Plan of Chongqing (Grant No. cstc2018jcyjAX0299) and the Open Foundation of Guangxi Key Laboratory of Processing for Non-ferrous Metals and Featured Materials (Grant No. 2020GXYSOF01).

Appendix A. Supplementary material

Supplementary data to this article can be found online at https://doi.org/10.1016/j.apsusc.2020.146214.

References

[1] Q. Ding, Y. Zhang, X. Chen, X. Fu, D. Chen, S. Chen, L. Gu, F. Wei, H. Bei, Y. Gao, M. Wen, J. Li, Z. Zhang, T. Zhu, R.O. Ritchie, Q. Yu, Tuning element distribution, structure and properties by composition in high-entropy alloys, Nature 574 (2019) 223–227.
[2] Y.F. Ye, Q. Wang, J. Lu, C.T. Liu, Y. Yang, High-entropy alloy: challenges and prospects, Mater. Today 19 (2016) 349–362.
[3] Y. Zhang, T.T. Zuo, Z. Tang, M.C. Gao, K.A. Dahmen, P.K. Liaw, Z.P. Lu, Microstructures and properties of high-entropy alloys, Prog. Mater. Sci. 61 (2014) 1–93.
[4] J. Gu, M. Song, Annealing-induced abnormal hardening in a cold rolled CrMnFeCoNi high entropy alloy, Scripta Mater. 162 (2019) 345–349.
[5] L. Chai, K. Xiang, J. Xia, V. Fallah, K.L. Murty, Z. Yao, B. Gan, Effects of pulsed laser surface treatments on microstructural characteristics and hardness of CrCoNi medium-entropy alloy, Philos. Mag. 99 (2019) 3015–3031.
[6] D.B. Miracle, O.N. Senkov, A critical review of high entropy alloys and related concepts, Acta Mater. 122 (2017) 448–511.
[7] Z. Li, S. Zhao, R.O. Ritchie, M.A. Meyers, Mechanical properties of high-entropy alloys with emphasis on face-centered cubic alloys, Prog. Aerosp. Sci. 102 (2019) 296–345.
[8] M. Wu, I. Baker, High strength and high ductility in a novel Fe40.2Ni11.3Mn30Al7.5Cr11 multiphase high entropy alloy, J. Alloy. Compd. 820 (2020) 11.
[9] A. Gali, E.P. George, Tensile properties of high- and medium-entropy alloys, Intermetallics 39 (2013) 74–78.
[10] Z. Wu, H. Bei, F. Otto, G.M. Pharr, E.P. George, Recovery, recrystallization, grain growth and phase stability of a family of FCC-structured multi-component equiatomic solid solution alloys, Intermetallics 46 (2014) 131–140.
[11] F. Guo, L. Jiang, Y. Ma, L. Liu, Z. Zhang, M. Yang, D. Zhang, F. Pan, Strengthening a dual-phase Mg-Li alloy by strain-induced phase transformation at room temperature, Scripta Mater. 179 (2020) 16–19.
[12] S.Y. Brechtl, X. Chen, Y. Xie, J.W. Ren, P.K. Qiao, S.J. Liaw, Zinkle, Towards a greater understanding of serrated flows in an Al-containing high-entropy-based alloy, Int. J. Plast. 115 (2019) 71–92.
[13] Y. Shi, B. Yang, X. Xie, J. Brechtl, K.A. Dahmen, P.K. Liaw, Corrosion of AlxCoCrFeNi high-entropy alloys: Al-content and potential scan-rate dependent pitting behavior, Corros. Sci. 119 (2017) 33–45.
[14] S.G. Ma, Creep resistance and strain-rate sensitivity of a CoCrFeNiAl0.3 high-entropy alloy by nanoindentation, Mater. Res. Exp. 6 (12) (2019) 8.
[15] D. Banerjee, J.C. Williams, Perspectives on titanium science and technology, Acta Mater. 61 (2013) 844–879.
[16] L.C. Zhang, L.Y. Chen, A review on biomedical titanium alloys: recent progress and prospect, Adv. Eng. Mater. 21 (2019) 1801215.
[17] L. Zhang, L. Chen, L. Wang, Surface modification of titanium and titanium alloys: technologies, developments, and future interests, Adv. Eng. Mater. 1901258 (2020).
[18] X. Qiu, C. Liu, Microstructure and properties of Al$_2$CrFeCoCuTiNi$_x$ high-entropy alloys prepared by laser cladding, J. Alloys Compd. 553 (2013) 216–220.
[19] S. Zhang, C.L. Wu, J.Z. Yi, C.H. Zhang, Synthesis and characterization of FeCoCrAlCu high-entropy alloy coating by laser surface alloying, Surf. Coat. Technol. 262 (2015) 64–69.
[20] H. Jiang, K. Han, D. Li, Z. Cao, Synthesis and characterization of AlCoCrFeNiNb$_x$ high-entropy alloy coatings by laser cladding, Crystals 9 (2019) 56.
[21] S. Zhang, C.L. Wu, C.H. Zhang, M. Guan, J.Z. Tan, Laser surface alloying of FeCoCrAlNi high-entropy alloy on 304 stainless steel to enhance corrosion and cavitation erosion resistance, Opt. Laser Technol. 84 (2016) 23–31.
[22] T. Wang, L. Zeng, Z. Li, L. Chai, T. Cheng, L. Zhang, V. Fallah, Q. Dong, Z. Yao, Influences of laser surface alloying with Cr on microstructural characteristics and hardness of pure Ti, Metall. Mater. Trans. A 50 (2019) 3794–3804.
[23] L. Chai, H. Wu, Z. Zheng, H. Guan, H. Pan, N. Guo, B. Song, Microstructural characterization and hardness variation of pure Ti surface-treated by pulsed laser, J. Alloys Compd. 741 (2018) 116–122.
[24] C. Guo, J. Zhou, J. Chen, J. Zhao, Y. Yu, H. Zhou, Improvement of the oxidation and wear resistance of pure Ti by laser cladding at elevated temperature, Surf. Coat. Technol. 205 (2010) 2142–2151.
[25] Z. Cai, X. Cui, Z. Liu, Y. Li, M. Dong, G. Jin, Microstructure and wear resistance of laser cladded Ni-Cr-Co-Ti-V high-entropy alloy coating after laser remelting processing, Opt. Laser Technol. 99 (2018) 276–281.
[26] C.C. Qu, J. Li, L.L. Bai, J.Z. Shao, R. Song, J.L. Chen, Effects of the thickness of the pre-placed layer on microstructural evolution and mechanical properties of the laser-clad coatings, J. Alloy Compd. 644 (2015) 450–463.
[27] J. Wang, T. Guo, J. Li, W. Jia, H. Kou, Microstructure and mechanical properties of non-equilibrium solidified CoCrFeNi high entropy alloy, Mater. Chem. Phys. 210 (2018) 192–196.
[28] L. Jiang, Y. Lu, Y. Dong, T. Wang, Z. Cao, T. Li, Annealing effects on the microstructure and properties of bulk high-entropy CoCrFeNiTi0.5 alloy casting ingot, Intermetallics 44 (2014) 37–43.
[29] Y. Zhang, T. Han, M. Xiao, Y. Shen, Effect of Nb content on microstructure and properties of laser cladding FeNiCoCrTi0.5Nb$_x$ high-entropy alloy coating, Optik 198 (2019) 163316.
[30] L. Chai, S. Wang, H. Wu, N. Guo, H. Pan, L. Chen, K.L. Murty, B. Song, α→β Transformation characteristics revealed by pulsed laser-induced non-equilibrium microstructures in duplex-phase Zr alloy, Sci. China Technol. Sci. 60 (2017) 1255–1262.
[31] S. Yoshida, T. Ikeuchi, T. Bhattacharjee, Y. Bai, A. Shibata, N. Tsuji, Effect of elemental combination on friction stress and Hall-Petch relationship in face-centered cubic high/medium entropy alloys, Acta Mater. 171 (2019) 201–215.
[32] S. Gao, T. Kong, M. Zhang, X. Chen, Y.W. Sui, Y.J. Ren, J.Q. Qi, F.X. Wei, Y.Z. He, Q.K. Meng, Z. Sun, Effects of titanium addition on microstructure and mechanical properties of CrFeNiTi$_x$ ($x = 0.2$-0.6) compositionally complex alloys, J. Mater. Res. 34 (2019) 819–828.
[33] Y. Yu, J. Wang, J. Li, H. Kou, W. Liu, Characterization of BCC phases in AlCoCrFeNiTi$_x$ high entropy alloys, Mater. Lett. 138 (2015) 78–80.
[34] Y. Zhang, Y.J. Zhou, J.P. Lin, G.L. Chen, P.K. Liaw, Solid-solution phase formation rules for multi-component alloys, Adv. Eng. Mater. 10 (2008) 534–538.
[35] D. Thoma, K. Nibur, K. Chen, K. Cooley, J. Dauelsberg, L. Hults, P. Kotula, The effect of alloying on the properties of (Nb, Ti)C_r2 C15 Laves phases, Mater. Sci. Eng. A 329 (2002) 408–415.
[36] K. Kumar, P. Hazzledine, Polytypic transformations in Laves phases, Intermetallics 12 (2004) 763–770.
[37] W.M. Tucho, P. Cuvillier, A. Sjolyst-Kverneland, V. Hansen, Microstructure and hardness studies of Inconel 718 manufactured by selective laser melting before and after solution heat treatment, Mater. Sci. Eng. A 689 (2017) 220–232.
[38] S. Guo, C. Ng, J. Lu, C.T. Liu, Effect of valence electron concentration on stability of

fcc or bcc phase in high entropy alloys, J. Appl. Phys. 109 (2011) 103505.

[39] C. Tong, M. Chen, J. Yeh, S. Lin, S. Chen, T. Shun, S. Chang, Mechanical performance of the Al_xCoCrCuFeNi high-entropy alloy system with multiprincipal elements, Metall. Mater. Trans. A 36 (2005) 1263–1271.

[40] M. Takeyama, C. Liu, Microstructure and mechanical properties of Laves-phase alloys based on Cr_2Nb, Mater. Sci. Eng. A 132 (1991) 61–66.

[41] K. Chen, S. Allen, J. Livingston, Factors affecting the room-temperature mechanical properties of $TiCr_2$-base Laves phase alloys, Mater. Sci. Eng. A 242 (1998) 162–173.

[42] H. Jiang, L. Jiang, D. Qiao, Y. Lu, T. Wang, Z. Cao, T. Li, Effect of niobium on microstructure and properties of the $CoCrFeNb_xNi$ high entropy alloys, J. Mater. Sci. Technol. 33 (2017) 712–717.

[43] F. He, Z. Wang, X. Shang, C. Leng, J. Li, J. Wang, Stability of lamellar structures in $CoCrFeNiNb_x$ eutectic high entropy alloys at elevated temperatures, Mater. Des. 104 (2016) 259–264.

[44] H. Zhang, Y. Pan, Y. He, Synthesis and characterization of FeCoNiCrCu high-entropy alloy coating by laser cladding, Mater. Des. 32 (2011) 1910–1915.